Materials Science & Engineering A 749 (2019) 137–147

Contents lists available at ScienceDirect

Materials Science & Engineering A

journal homepage: www.elsevier.com/locate/msea

Small punch creep testing of thermally sprayed Stellite 6 coating: A comparative study of as-received vs post-heat treatment

G.A. Jackson[a], M. Bai[b], Z. Pala[c], T. Hussain[a,*], W. Sun[a]

[a] Faculty of Engineering, University of Nottingham, University Park, Nottingham NG7 2RD, UK
[b] Department of Materials Science and Engineering, University of Sheffield, Sheffield S1 3JD, UK
[c] GE Aviation, Beranovych 65, Prague, Czech Republic

ARTICLE INFO

Keywords:
Small punch creep
HVOF
Stellite 6
Creep
Fracture
Mechanical properties

ABSTRACT

Thermally sprayed Stellite 6 coatings offer high wear and corrosion-erosion resistance at high temperature but the creep behaviour of such coatings is not well understood. In this paper, the microstructure and creep behaviour of a HVOF Stellite 6 coating was investigated. The coating was tested in the as-sprayed condition and after an isothermal heat-treatment of 1 h at 1050 °C. The as-sprayed coating comprised FCC Co-Cr-W solid solution with 2–3 wt% HCP phase, whereas the heat-treated coating comprised FCC Co-Cr-W solid solution, 11 wt% $M_{23}C_6$ carbides and 7 wt% M_7C_3 carbides. Small punch creep tests were conducted at 700 °C on the as-sprayed and heat-treated coatings. The heat-treated coating exhibited minimum steady-state strain rates approximately 2 orders of magnitude lower than the as-sprayed coating when tested at similar loads, leading to times to failure approximately two orders of magnitude longer for the heat-treated coating within the selected load range. Fracture analysis showed cracking along powder particle boundaries was the main mode of cracking in the as-sprayed coating whereas for the heat-treated coating, fracture along the carbide / matrix interface was the main fracture mechanism.

1. Introduction

Thermally sprayed coatings are widely used to extend the lifetime of substrate components in power generation [1–3]. Hard-facing alloys, such as Cobalt-based Stellite 6, offer high wear and corrosion-erosion resistance at high temperature, which makes them attractive candidates for use as thermally sprayed coatings in power generation [4–6]. The suitability of Stellite 6 was demonstrated by Hjornhede et al. [6] who reported that Stellite 6 exhibited the lowest amount of degradation compared to other Co, Fe and Ni-based alloys when exposed to hot erosion-corrosion environments.

In high temperature environments, the durability of thermally sprayed coatings is significantly influenced by creep: stress induced cracking, buckling and delamination have all been shown to be influenced by creep [7–9]. Hence, understanding the creep properties of thermally sprayed coatings is important for high temperature applications. However, thermally sprayed coatings are typically too thin for traditional creep test methods such as uni-axial creep testing. An alternative test method suitable for thin specimens is the small punch test method. The small punch test can be used in a constant load (small punch creep) or constant displacement (small punch tensile) configuration and has been used to evaluate the mechanical properties of thermally sprayed MCrAlY coatings [10–14] and a nickel aluminide diffusion coatings [15].

The small punch test allowed the influence of coating microstructure on the mechanical properties of thermally sprayed coatings to be investigated [11–13], which presents the possibility to improve the creep resistance of thermally sprayed coatings by developing coating microstructures. This can be achieved through varying the deposition method or through post-process heat treatments such as laser re-melting [16–18] and isothermal annealing [19,20]. Temperatures above 1000 °C are typically required for isothermal annealing to ensure homogenisation of the microstructure and reduction in porosity [19–21]. Comparatively, laser re-melting is a more complex process than isothermal annealing and can lead to dissolution of the substrate into the coating which makes it a less attractive post-process heat treatment.

In this paper, the relationship between microstructure, creep behaviour and creep fracture of a free-standing Stellite 6 high velocity oxy-fuel (HVOF) coating in the as-sprayed and heat-treated condition (1 h at 1050 °C under vacuum) was investigated. The creep behaviour of the as-sprayed and heat-treated HVOF Stellite 6 coating was

* Corresponding author.
E-mail address: tanvir.hussain@nottingham.ac.uk (T. Hussain).

https://doi.org/10.1016/j.msea.2019.02.030
Received 25 January 2019; Received in revised form 7 February 2019; Accepted 8 February 2019
Available online 10 February 2019

investigated through small punch creep tests conducted at 700 °C. The exposure conditions were chosen to reflect the temperatures in the superheaters of the latest generation of steam generators operating under ultra-supercritical conditions with biomass as a fuel where metal temperatures will be in excess of 650 °C (22). The creep behaviour was characterised by minimum creep strain state and creep rupture life. The macroscopic and microscopic fracture patterns of the as-sprayed and heat-treated coatings were then investigated with reference to the coating microstructures.

2. Materials and methods

2.1. Materials and HVOF thermal spraying

Stellite 6 powder was provided by Kennametal Stellite Inc. with median diameter (D50) of 38 µm, as determined by a Malvern Master Sizer (Malvern, UK), and a composition of Co–28.3Cr–4.8W–2.2Ni–1.5Fe–1.2Si–1.2C. The powder was sprayed onto mild steel substrates 1.5 mm thick, 60 mm long and 25 mm wide using a MetJet IV liquid fuel-based HVOF system developed by Metallisation Ltd. UK. The nozzle length was 100 mm, the stand-off distance was 356 mm and the flow rates of kerosene and oxygen were 476 ml/min and 920 l/min respectively. Nitrogen was used as a carrier gas for the powder. The coatings were deposited to a thickness of approximately 700 µm and subsequently detached from the substrates by bending around a mandrel. The free standing coatings surfaces were ground on 240 grade SIC papers and discs of 8 mm diameter were then cut from coatings via electric discharge machining. Vacuum heat treatment was carried out on half of the free-standing samples at 1050 °C for one hour in an Elite Thermal Systems TVH12 vacuum tube furnace held at approximately 10^{-9} bar followed by furnace cooling to room temperature over a period of 6 h. The as-sprayed and heat-treated discs were then subject to a final stage polishing on 1200 grade SiC paper to a final thickness of ~500 µm.

2.2. Microstructural characterisation

Cross-sections of the feedstock Stellite 6 powder and as-sprayed and heat-treated HVOF coatings, both before and after Small Punch Creep (SPC) testing, were mounted, ground and polished to 1 µm finish. The polished feedstock powder and as-sprayed coating were electro-polished in a solution of 1 g oxalic acid (molecular weight = 90.04 g/mole) and 100 ml di-ionised water. Microstructural analysis was carried out using an FEI Quanta600 (Oregon, USA) scanning electron microscope (SEM) equipped with a Bruker X-Flash (Massachusetts, USA) energy dispersive X-ray spectroscopy (EDS) detector.

X-ray diffraction (XRD) measurements of the as-sprayed and heat-treated coatings were done in a Siemens D500 XRD system (Germany), with a vertical θ-2θ diffractometer in Bragg-Brentano set-up, using Cu-Kα radiation and scintillation point detector with secondary monochromator. The scanned 2θ range was from 20° to 120° with 0.05° step size and 20 s of counting time in each step. TOPAS software package (Bruker AXS, Germany) was employed for Rietveld analysis [23].

2.3. Microhardness testing

Microhardness measurements were carried out on polished cross-sections of the as-sprayed and heat-treated Stellite 6 HVOF coatings. All measurements conformed to ASTM E92 and were made using a 300 gf load and dwell time of 10 s. An average of 5 measurements was calculated for each coating and the error was taken as the standard deviation.

2.4. Small punch creep testing

Constant-load SPC tests were carried out on a custom built SPC rig installed on a Tinius Olsen (Surrey, UK) H5KS single column materials testing machine. A schematic diagram of the rig is shown in Fig. 1. The load was applied through a 2.5 kN load cell and the punch head displacement was measured by two LDVT's. A three tier, 3 kW furnace was used to heat the specimens at a heating rate of 5 °C/min. Three K-type thermocouples, accurate to 5 °C, were used to measure the furnace temperature in the top, middle and bottom tiers. The three thermocouples were connected to a Severn Thermal Solutions temperature controller which controlled the temperature to ± 2 °C, giving an overall temperature tolerance of ± 7 °C. All tests were carried out in a temperature controlled room held at 21 °C. The samples were heated to temperature and held at temperature for 5 h prior to the application of the load. Full details on the SPC rig can be found at [24].

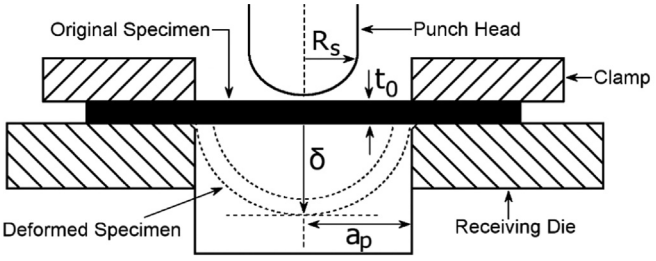

Fig. 1. Schematic cross section of the small punch creep rig showing the application of load through a hemispherical punch head and resultant specimen displacement (δ) where a_p, R_s and t_0 are the radius of the receiving hole (2 mm), punch head radius (1 mm) and original specimen thickness (0.5 mm) respectively.

3. Calculation of strain and material properties

During SPC testing, a constant load is applied to a specimen through a hemi-spherical punch head, as indicated in Fig. 1, which induces a complex bi-axial stress state in the specimen. Accurate calculation of the bi-axial stress and strain in a SPC specimen is not possible without finite element modelling. As such, analytical analysis of SPC testing employs semi-empirical solutions to calculate the equivalent uni-axial stress (MPa) and equivalent uni-axial strain from the applied load (N) and specimen displacement (mm) respectively [25].

The load was converted to equivalent uni-axial stress (σ_e) (MPa) using the following equation provided by the CEN workshop agreement [25]:

$$\frac{F}{\sigma_e} = 3.33 \quad K_{sp} a_p^{-0.2} R_s^{1.2} t_0 \tag{1}$$

where a_p (mm), R_s (mm) and t_0 (mm) are the radius of the receiving hole, punch head radius and specimen thickness respectively, as shown in Fig. 1. F is the load (N) and K_{sp} is a non-dimensional correction factor used to correlate SPC data with uni-axial testing data. K_{sp} is reported in the CEN workshop agreement [25] to be between 1.2 and 1.3 but has also been reported as 0.6–0.8 for single crystal CMSX-4 ref [26]. In this study, a K_{sp} value of 1 was used in line with the CEN workshop recommendations for materials where uni-axial test data does not exist.

The specimen displacement (δ) was converted to equivalent uni-axial strain (ε) using the solution provided by Li et al. [27] which was semi-empirically derived from Chakrabarty's membrane stretching theory [28]. The minimum steady state strain rate ($\dot{\varepsilon}_{min}$) was calculated using a 1/5th moving average.

$$\varepsilon_q = 0.20465 \quad \delta + 0.12026 \quad \delta^2 - 0.00950 \quad \delta^3 \tag{2}$$

Relationships between the equivalent uni-axial stress (σ_e), the equivalent uni-axial minimum steady-state strain rate ($\dot{\varepsilon}_{min}$) and the time to failure (t_f) can be obtained from the following three equations. These equations are used to describe the material creep behaviour following SPC testing at 700 °C.

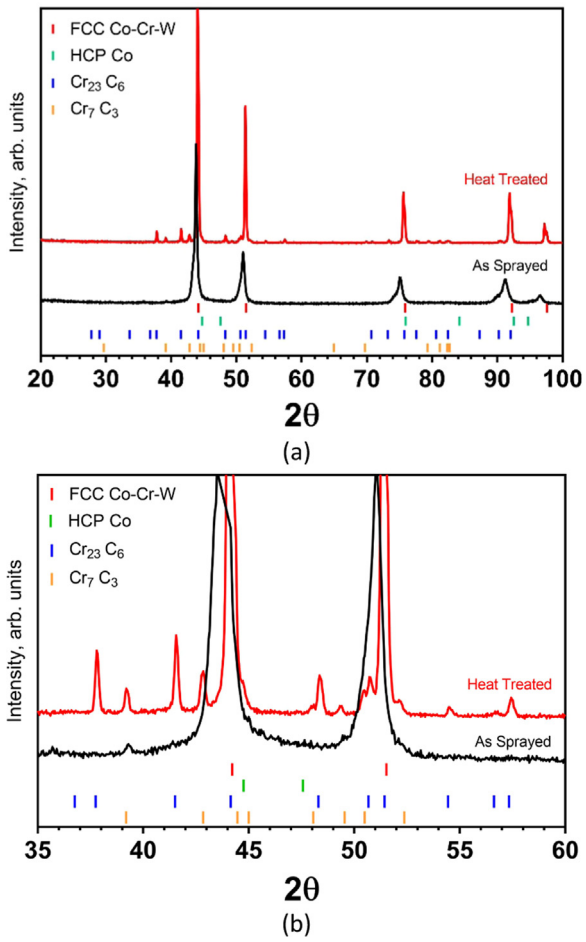

Fig. 2. XRD patterns of the as-sprayed and heat-treated Stellite 6 coatings between 2θ values of (a) 20–100° and (b) 35–60°. The as-sprayed coating comprised FCC Co-Cr-W and 2–3 wt% HCP Co, whereas the heat-treated coating comprised FCC Co-Cr-W, 11 wt% $M_{23}C_6$ and 7 wt% M_7C_3 as calculated by Rietveld analysis.

Norton Steady-State Power Law:

$$\dot{\varepsilon}_{min} = B\sigma_e^{\,n} \tag{3}$$

Creep Rupture Power Relationship:

$$t_f = \frac{1}{M\sigma^{\chi}} \tag{4}$$

Monkman-Grant Relationship:

$$t_f = K_1 \dot{\varepsilon}_{min}^{\,-m} \tag{5}$$

where B, n, M, χ, K_1 and m are temperature dependent material properties.

4. Results

4.1. Characterisation of HVOF Stellite 6 coatings

4.1.1. XRD analysis

XRD diffraction patterns of the as-sprayed [22] and heat-treated Stellite 6 coatings are shown in Fig. 2. The phases present in the as-sprayed Stellite 6 were reported by Pala et al. [22] as almost exclusively FCC Co-Cr-W solid solution with 2–3 wt% HCP Co-based phase, as measured by quantitative Rietveld analysis of XRD data. Pala et al. [22] also reported the Stellite 6 feedstock powder to comprise approximately 91 wt% FCC and 9 wt% HCP phase which demonstrated that the as-sprayed coating retained, in general, the original powder microstructure. The heat-treated coating exhibits sharp FCC Co-Cr-W reflections and new diffraction maxima corresponding to phases with similar lattice parameters to a $Cr_{23}C_6$ carbide and a Cr_7C_3 carbide. The phase fractions were 11 wt% cubic $M_{23}C_6$ carbide and 7 wt% orthorhombic M_7C_3 as refined by Rietveld analysis. There is a clear reduction in diffraction profile width of the main phase between the patterns of as-sprayed and heat-treated samples, most likely the result of an alleviation in microstrains during heat treatment and grain coarsening. At the same time, there is a shift to higher 2θ angles of FCC phase (see Fig. 2b) indicating decrease in the lattice parameter that is obviously explained by the chromium transfer from the matrix to the carbides; chromium has higher atomic radius than cobalt and, thus, less chromium in FCC matrix lead to the decrease of FCC lattice parameter.

4.1.2. Microstructural investigation

BSE micrographs of a cross-sectional etched Stellite 6 powder particle are shown in Fig. 3. The powder exhibits a dendritic microstructure, similar to that previously reported elsewhere [29,30]. BSE micrographs of the as-sprayed Stellite 6 coating, shown in Fig. 4, show the interdendritic powder microstructure was retained in parts of the as-sprayed coating through partially melted powder particles, as indicated by A, which underwent varying degrees of deformation during spraying. The retention of the powder particle microstructure supports the XRD analysis that the as-sprayed coating retained, in general, the original powder microstructure. The boundaries of the retained powder

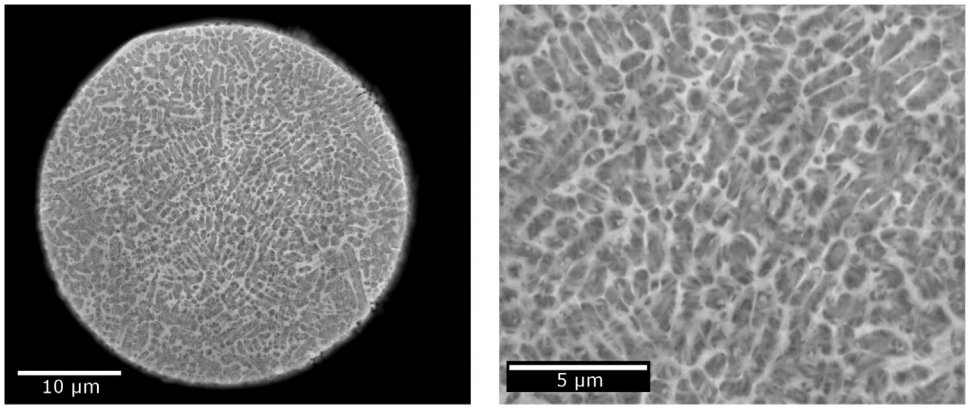

Fig. 3. BSE micrographs of an etched Stellite 6 powder particle. The powder particle exhibits a dendritic microstructure which was retained in the as-sprayed coating (Fig. 4).

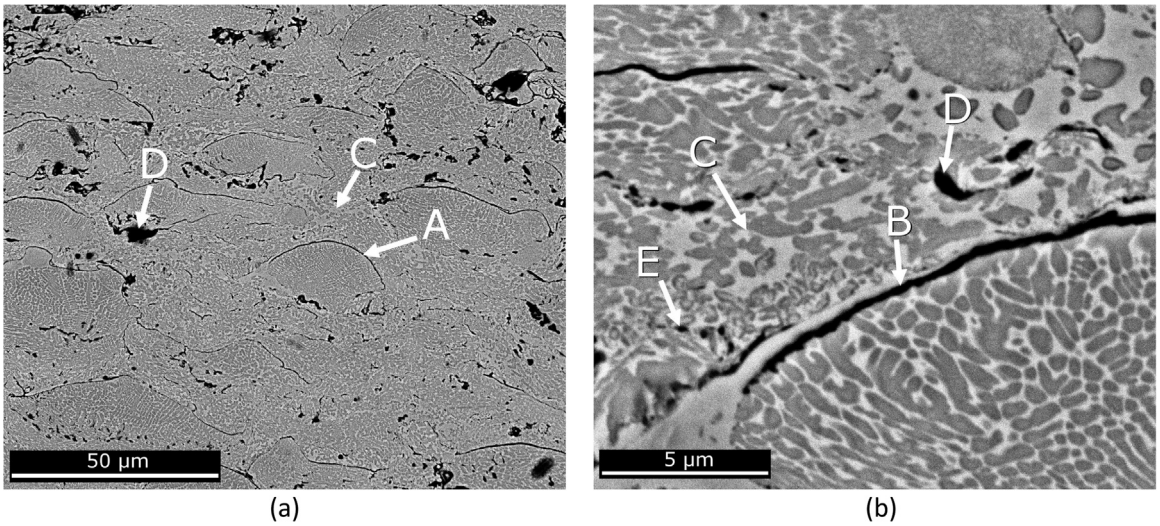

Fig. 4. BSE micrographs of the as-sprayed HVOF Stellite 6 coating after electro-etching in oxalic acid. The coating consists of partially melted powder particles (A), thin bands of oxides/pores (B), regions that melted under spraying and recrystallized under cooling (C), large pores (D) and small pores (E).

particles are typically highlighted by thin black bands, as indicated by B, which are either oxides or pores that formed during thermal spraying. The powder particles are inter-connected by regions where the alloy fully melted during spraying and re-solidified under cooling, as indicated by C. These regions were described by Kong et al. [29] to be unresolvable in an SEM due to a monocrystalline structure that formed due to the high cooling rate experienced by the molten alloy: approximately 10^7 K s^{-1} [31]. There also exists large pores, as indicated by D, and small discrete pores, as indicated by E. The porosity / oxide level in the as-deposited coating is approximately 5 vol% as measured by image analysis. The elemental composition of the as-sprayed coating, determined from EDX analysis a 180 × 180 μm area, was as follows:: Cr 30.7 ± 0.3, Si 1.4 ± 0.1, Fe 2.3 ± 0.1, W 6.2 ± 0.3, Co bal. (in wt%). Carbon was not included in the EDX measurement and the values have been normalised to reflect this. The composition of the as-sprayed coating matches well with the composition of the feedstock powder.

BSE images of the Stellite 6 coating following heat treatment at 1050 °C for 1 h under vacuum are shown in Fig. 5. The heat treatment significantly reduced the level of porosity in the coating to approximately 1 vol%, as measured by image analysis, and has eliminated the large black pores observed in the as-sprayed coating. This 'healing' effect of heat treatment on coatings has been previously reported [10,20,24].

The partially melted powder particles, indicated by A, are still observable in the heat-treated coating by thin bands of small discrete oxides/pores, such as those indicated by F, that exist at the powder particle boundaries. EDX analysis showed the majority of these features to be pores rather than oxides. The microstructure of the heat-treated coating is homogenous. EDX and EBSD analysis confirmed the coating comprised: light contrast FCC Cr-Co-W solid solution; dark grey M_7C_3 carbides, indicated by G; and light grey $M_{23}C_6$ carbides indicated by H. There is also a fine dispersion of W rich regions which appear bright in the BSE images, indicated by I. The composition of each phase, as measured by EDX, is shown in Table 1. It is clear that the concentration of W in the $M_{23}C_6$ carbides is higher than in the M_7C_3, which explains why the $M_{23}C_6$ carbide exhibited a brighter contrast in the BSE image.

The as-sprayed and heat-treated coatings exhibited an average microhardness (HV_{300gf}) of 662 ± 14 and 486 ± 9 respectively. The heat-treated coating exhibited a significantly lower hardness than the as-sprayed coating, despite the precipitation of numerous carbides, indicating that the depletion of the matrix by elements that formed

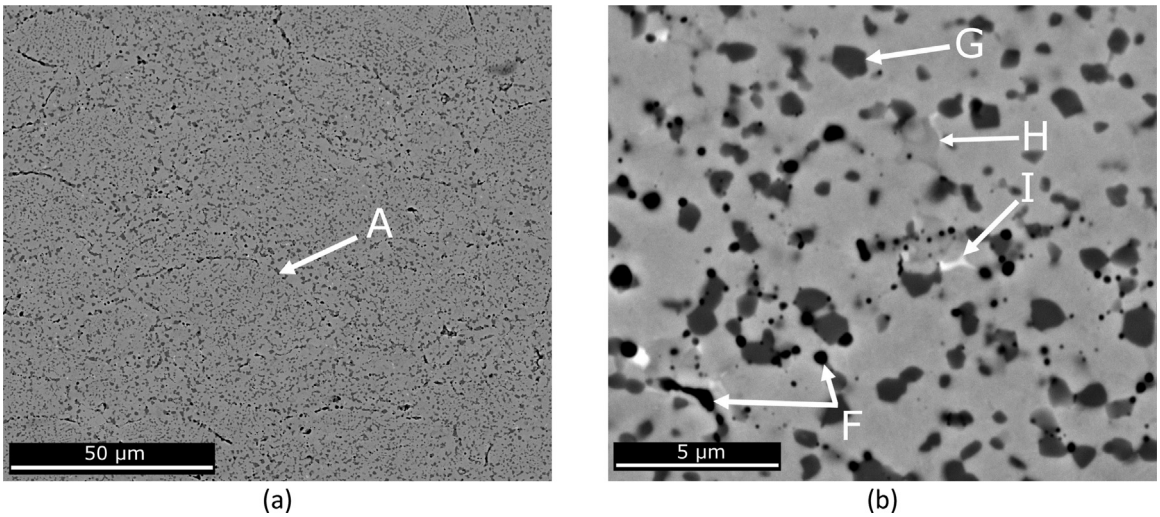

Fig. 5. BSE micrographs showing the microstructure of the HVOF Stellite 6 coatings following vacuum heat treatment at 1050 °C for 1 h. The boundaries of partially melted powder particles (A) can be identified, as well as M_7C_3 carbides (G), $M_{23}C_6$ carbides (H) and a fine dispersion of W rich regions (I).

Table 1
EDX measurements of selected phases. Average of 4 measurements. Error shown is the standard deviation.

	Composition (wt%)					
Phase	**Co**	**Cr**	**W**	**Fe**	**Ni**	**Si**
FCC Co Cr W	68.3 ± 5.0	21.3 ± 1.6	4.4 ± 1.4	2.3 ± 0.3	2.7 ± 0.3	1.0 ± 0.2
M_7 C_3 carbides **(G)**	30.4 ± 2.5	64.6 ± 4.0	2.3 ± 0.3	1.3 ± 0.2	1.0 ± 0.2	0.4 ± 0.1
M_{23} C_6 carbides **(H)**	34.7 ± 2.5	52.9 ± 3.7	9.4 ± 0.7	1.4 ± 0.2	1.2 ± 0.2	0.4 ± 0.1
W rich regions **(I)**	47.8 ± 3.4	31.1 ± 2.3	14.7 ± 1.1	1.4 ± 0.2	2.2 ± 0.2	2.9 ± 0.4

carbides is the dominant factor determining the hardness overruling the effect of carbide presence. Moreover, it can be assumed that the hardness (HV) of the coatings follows the Hall–Petch relationship:

$$HV = HV_0 + C\lambda^{-0.5} \quad (6)$$

where HV_0 is original hardness, C is a constant and λ is the interparticle distance [32]. The interdendrite arm spacing in the as-sprayed coating is lower than the inter-carbide spacing in the heat-treated coating (approximately < 1 μm and 1–2 μm respectively), which provides further explanation as to why the heat-treated coating exhibits a lower hardness than the as-sprayed coating.

4.2. Small punch creep results

Representative time-displacement curves obtained from the as-sprayed and heat-treated coatings during SPC testing at 700 °C are shown in Fig. 6. The stresses shown are calculated using Eq. (1). Each curve exhibits a primary region consisting of a large initial deformation followed by a reduction in the displacement rate, a secondary steady-state region where the displacement rate is approximately constant, and a tertiary region where the displacement rate accelerates leading to failure. The initial displacements following the application of the load, the overall displacements at failure and the steady-state displacement rates increased as the loads were increased, whereas the times to failure decreased. As such, it is clear both the as-sprayed and heat-treated HVOF Stellite 6 coatings exhibited typical creep behaviour during SPC testing at 700 °C. The heat-treated coating exhibited a higher resistance to creep than the as-sprayed coating and so was subjected to higher loads in order to obtain similar times to failure for both coatings.

Fig. 7 shows log-log plots correlating the equivalent uni-axial minimum steady-state strain rate, equivalent uni-axial stress and time to failure for the as-sprayed and heat-treated coatings. Linear relationships have been drawn to allow parameters for the Norton steady-state power law, the creep rupture power law and the Monkman-Grant relationship can be calculated. The calculated values are shown in Table 2.

The heat-treated coating exhibited a lower, by approximately two orders of magnitude, minimum steady-state strain rate (for any given stress) compared to the as-sprayed coating. This resulted in the heat-treated coating exhibiting times to failure approximately two orders of magnitude greater than the as-sprayed coating. The time to failure for any given strain rate remained consistent between the as-sprayed and heat-treated coatings, demonstrating the total strain to failure remained consistent.

The rate at which the minimum steady-state strain rate increased with stress, and the rate at which the time to failure increased with stress, described respectively by the Norton power law constant 'n' and rupture powder law constant 'χ', was consistent between the as-sprayed and heat-treated coatings. This indicates the dominant creep mechanism at 700 °C was similar for both coatings.

4.3. Failure of SPC specimens

In order to further understand the difference in creep behaviour between the as-sprayed and heat-treated coatings it is necessary to evaluate the fracture behaviour of both coatings. SE images of the as-sprayed and heat-treated coatings following SPC testing at 700 °C are shown in Fig. 8. The as-sprayed and heat-treated specimens shown were tested at 102 and 127 MPa respectively, and exhibited similar minimum steady-state strain rates during testing, approximately 2×10^{-7} s^{-1}. These samples were chosen to ensure that the fracture behaviour being observed occurred whilst both coatings experienced similar strain rates. Thus allowing accurate comparisons to be drawn.

The centre of both specimens fractured and detached during testing; the resultant holes correspond to the size of the punch head and are approximately 2 mm in diameter for both specimens feature. Radial cracks are observable on both specimens which have been reported to initiate in the centre of SP specimens and are associated with brittle cracking at low displacements [24,33,34]. The black boxes in Fig. 8a and b indicate the areas shown at higher magnification in Fig. 8(c and

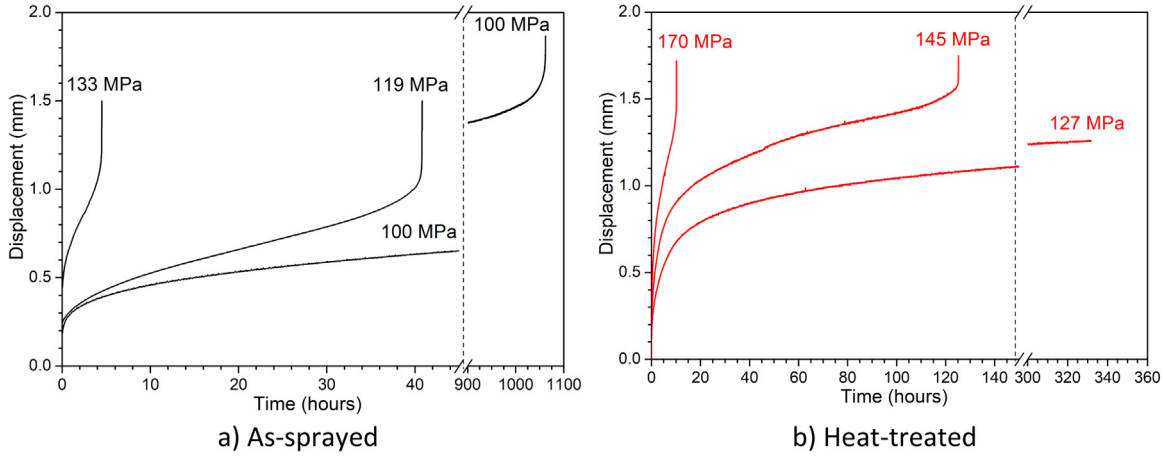

Fig. 6. Representative SPC displacement-time curves of the as-sprayed and heat-treated Stellite 6 coatings tested at 700 °C. Both coatings exhibit typical creep behaviour at 700 °C.

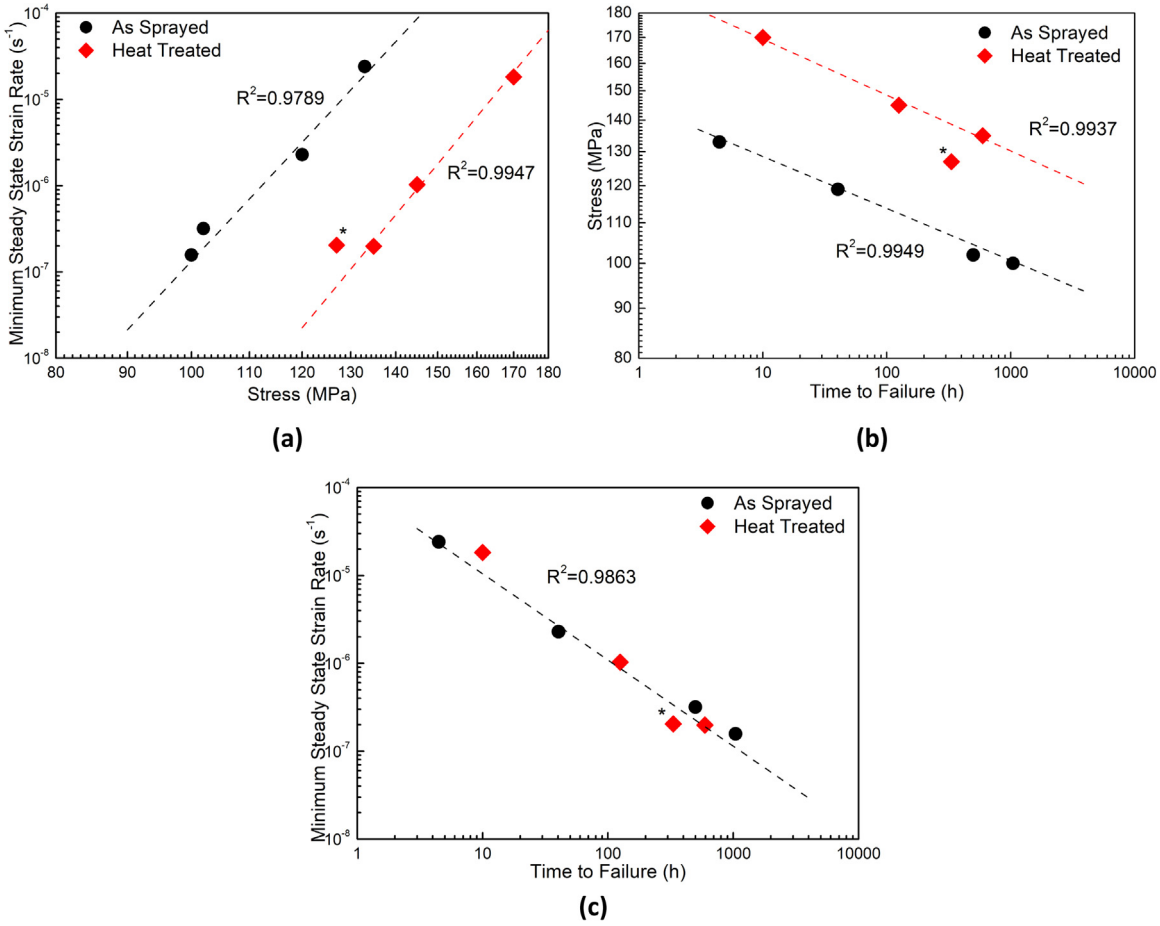

Fig. 7. (a) Minimum steady-state strain rate vs stress, (b) stress vs time to failure and (c) minimum steady state-strain rate vs time to failure for the as-sprayed and heat-treated Stellite 6 coatings at 700 °C as calculated from analysis of SPC testing.

Table 2
Parameters for the Norton power law, creep rupture power law and modified Monkman-Grant relationship for the as-sprayed and heat-treated coatings at 700 °C. Values calculated from the graphs shown in Fig. 7.

	Norton power law		Rupture power law		Monkman-Grant relationship	
	B (s^{-1} MPa^{-n})	n	M (h^{-1} $MPa^{-\chi}$)	χ	K_1 ($h\,s^m$)	m
As-sprayed	2.1×10^{-42}	17.4	1.61×10^{-40}	18.4	1.1×10^{-4}	1.02
Heat-treated	1.3×10^{-48}	19.4	1.55×10^{-40}	17.4		

d) and Fig. 8(e and f) respectively.

The fracture surface of the as-sprayed coating following SPC testing at 700 °C and 102 MPa is shown in Fig. 8(c and d). There are a large number of powder particles, as well as craters that mirror the shape of powder particles, which can be clearly identified on the fracture surface. The smooth surface of these features suggests the boundaries of powder particles were weak areas that acted as paths for continuous crack propagation. The remaining fracture surface exhibits a high density of small surface features which indicates a different type of crack propagation throughout the bulk of the as-sprayed specimen. This crack propagation is detailed in Fig. 9.

The fracture surface of the heat-treated coating tested at 700 °C and 127 MPa is shown in Fig. 8(e and f). The fracture surface features a high density of small surface features, similar to the as-sprayed specimen, which are detailed in Fig. 10. It is not possible to clearly identify powder particles on the fracture surface of the heat-treated specimen but craters similar to those observed on the fracture surface of the as-sprayed specimen are visible. These craters indicate that the powder particle boundaries remain a preferential crack path in the heat-treated specimen; however, the craters exhibit a rough surface which indicates a different type of crack propagation compared to the as-sprayed specimen.

In order to investigate the crack propagation behaviour in the tested SPC specimens, the areas indicated by the black boxes in Fig. 8(a and b) were cut from the specimens and mounted so that cross-sections of the cracks could be studied. BSE micrographs of a cross section taken from as-sprayed specimen are shown in Fig. 9. There is clear evidence of crack propagation along the powder particle boundaries, as indicated by A in Fig. 9(b). This appears to be the main mode of crack propagation in the as-sprayed coating. Fig. 9b and c show a secondary mode of crack propagation wherein a crack has propagated through a powder particle. The crack has propagated along the dendrite phase boundaries, as indicated by B.

Micrographs of a cross section through the heat-treated specimen are shown in Fig. 10. There is clear evidence of crack propagation along a powder particle boundary, as indicated by A, which corresponds to the craters observed on the fracture surface of the heat-treated coating, shown in Fig. 8(e and f). The shape of the crack path along the powder boundary is irregular, which explains why the craters on the fracture surface exhibited a non-smooth, irregular surface that was different to the smooth surface of the craters observed on the fracture surface of the as-sprayed specimen. Fig. 10c and d show how crack propagation occurred in regions not associated with a powder particle boundary. Considering the low density of powder particles and craters on the fracture surface of the heat-treated specimen, the types of crack propagation observed in these regions can be considered the main modes of

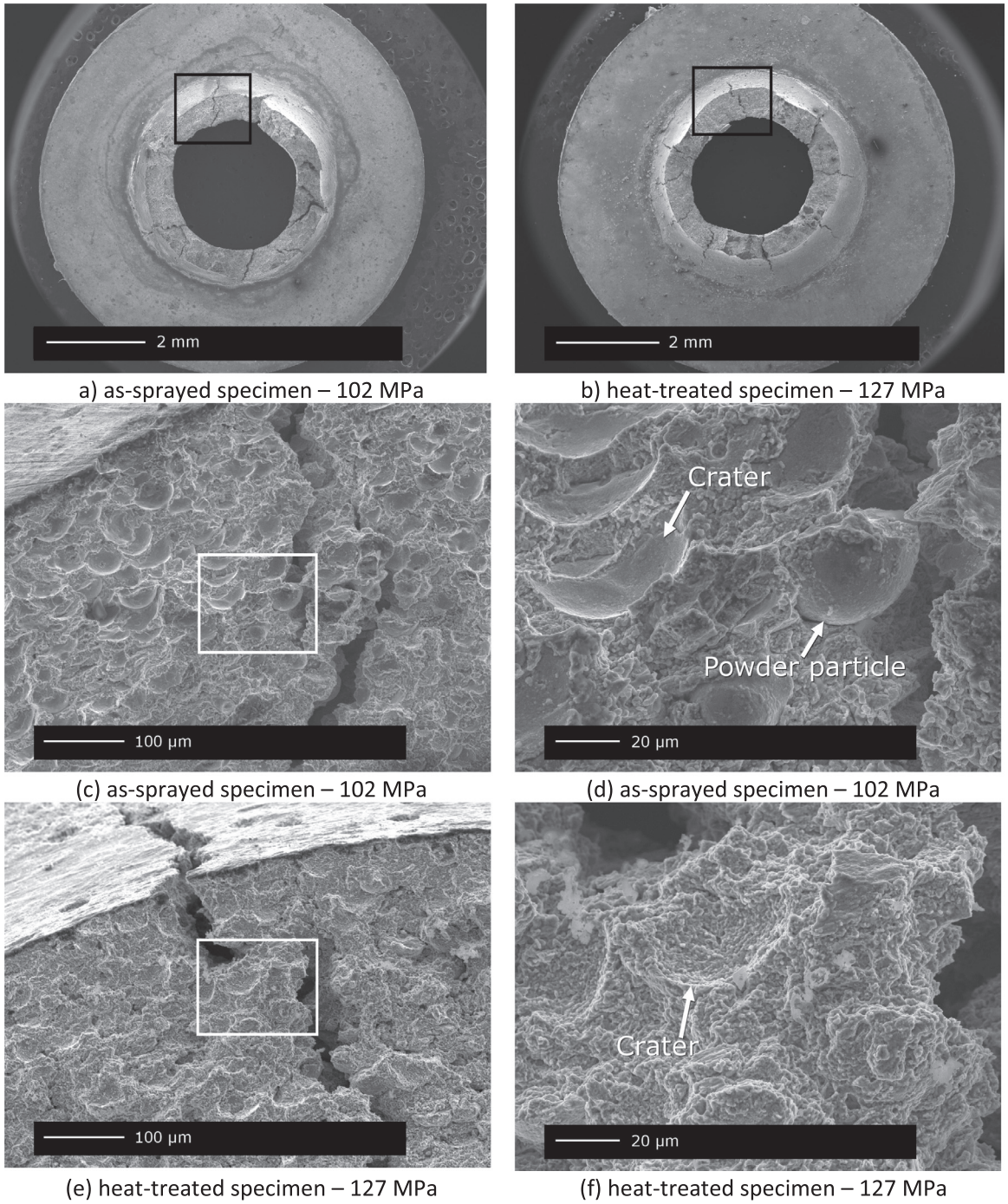

Fig. 8. SE micrographs of the as-sprayed and heat-treated Stellite 6 coating specimens following SPC testing at 700 °C. The macroscopic fracture patterns are shown in (a) and (b) for the as-sprayed and heat-treated coatings respectively. Both specimens exhibit circumferential and radial cracking. The black boxes indicate the areas shown at higher magnification in (c and d) and (e and f). The fracture surface of as-sprayed Stellite 6 specimen is shown in (c) and (d). A high density of partially melted powder particles, as well as craters which correspond to pull-out of powder particles, can be identified on the fracture surface. The fracture surface of heat-treated Stellite 6 coating specimen is shown in (e) and (f). Craters, due to powder particle pull-out, can be identified.

crack growth in the heat-treated Stellite 6 coating. There is evidence of crack propagation along the carbide/matrix interface, as indicated by B, and evidence of crack propagation either through a carbide, or along a carbide/carbide interface, as indicated by C. There is also evidence of pores forming at the carbide/matrix and carbide/carbide interfaces, as indicated by D, which is evidence of how the observed cracks developed under tensile loading.

5. Discussion

Considering the SPC behaviour of the coatings first, the minimum steady-state strain rates observed for the heat-treated coating were approximately 2 orders of magnitude lower than those observed for the as-sprayed coating. This demonstrates that the vacuum heat-treatment at 1050 °C, and the subsequent changes in microstructure, resulted in a marked increase in creep resistance for the Stellite 6 coating. In order to understand the change in creep behaviour it is necessary to first consider the microstructural evolution of the Stellite 6 coating.

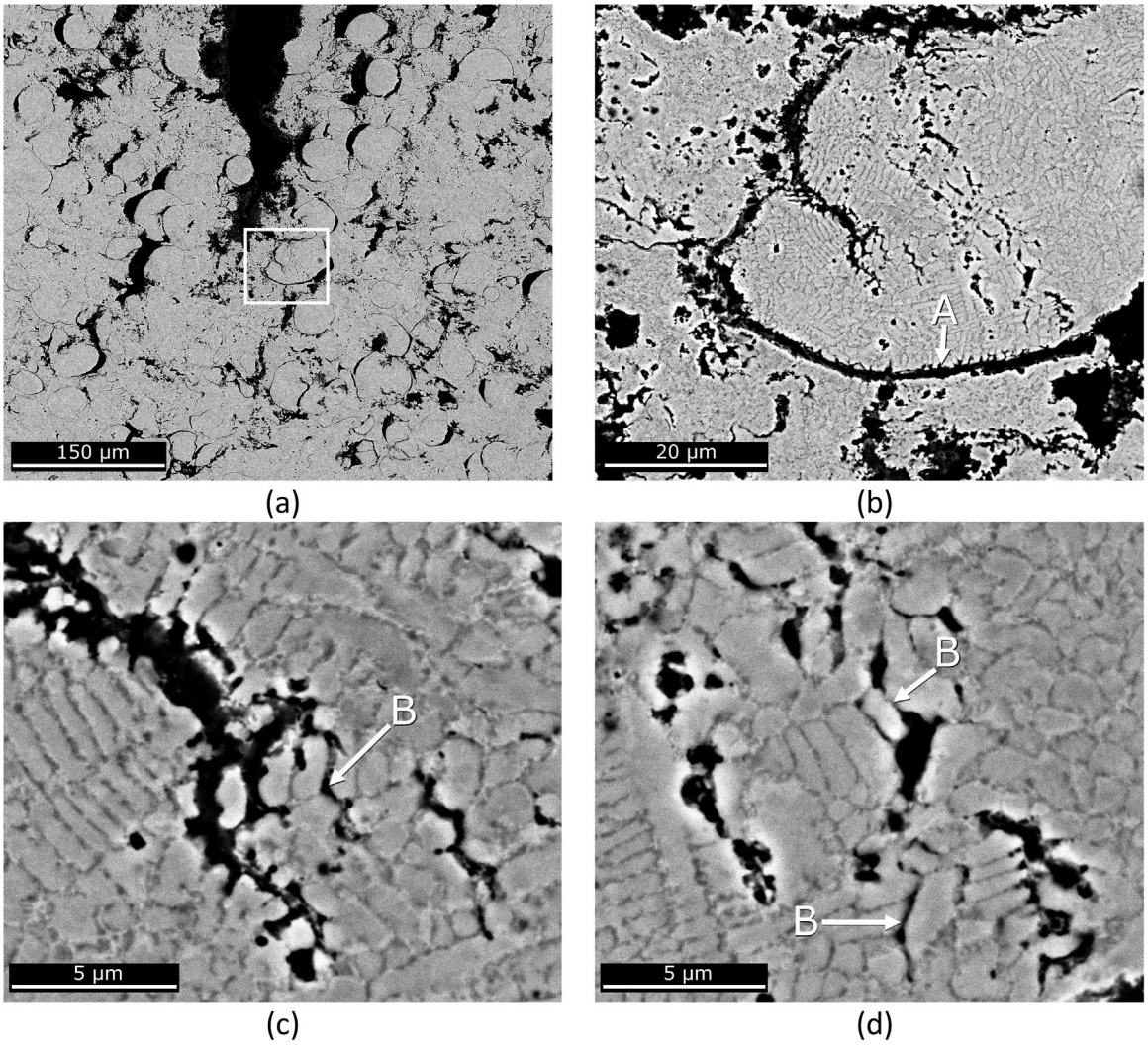

Fig. 9. BSE micrographs of the as-sprayed Stellite 6 coating following SPC testing at 700 °C and 102 MPa, showing a cross-section of the area highlighted in Fig. 8a. The letter A indicates cracking along a powder particle boundary and B indicates cracking along the dendrite phase boundaries.

The as-sprayed coating was comprised almost exclusively of FCC Co-Cr-W solid solution with no carbides identified by Rietveld analysis. However, it is possible that carbides were present in the as-sprayed coating but at concentrations below the detection limit of XRD; approximately 1 wt%. The microstructure of the as-sprayed coating is consistent with the microstructures previously reported for similar coatings [22,29,30,35]. The lack of carbides is commonly associated with the high cooling rates experienced by the alloy during HVOF spraying; approximately 10^7 K s^{-1} [31]. The high cooling rates typically cause residual stresses in as-sprayed HVOF coatings [36] but the impact of residual stresses on creep properties is not taken into account in this study. While the residual stresses in as-sprayed HVOF coatings of metallic materials are compressive, due to the high velocity of impinging particles and resulting peening effect during the coating built-up, the stresses will be reduced during annealing. Whereas the significance of residual stresses in, mainly high cycle, fatigue life is firmly established [37] their effects on creep, that itself falls under relaxation processes, is more complex and for the sake of clarity, it is considered as beyond the scope of this article.

The heat-treated coating comprised FCC Co-Cr-W solid solution with M_7C_3 and $M_{23}C_6$ type carbides. M_7C_3 type carbides are widely reported in laser clad, cast and hot isostatically pressed (HIPped) Stellite 6 alloys [32,38–40]. $M_{23}C_6$ type carbides are not commonly reported but have been observed with the addition of Mo, Y and Si [41,42]. Thermodynamic calculations (not presented in this paper) predict $M_{23}C_6$ carbides to form below approximately 950 °C. Hence, the presence of $M_{23}C_6$ type carbides in the heat-treated Stellite 6 coating is most likely the result of slow furnace cooling following the isothermal heat-treatment at 1050 °C.

The precipitation of carbides in the heat-treated coating was the most significant phase change during heat-treatment. As such, it can be concluded that the precipitation of carbides, as well as the corresponding decrease in hardness, increased the creep resistance of the Stellite 6 coating. This is consistent with the well-documented observation that carbides increase the strength of Co-base alloys [43,44] but contradicts the findings that a loss of hardness can decrease creep rupture lifetime [45]. As such, it appears the loss of creep lifetime due to a loss of hardness was far off-set by the increased creep resistance due to the precipitation of carbides.

The precipitation of carbides was not the only microstructural difference between the as-sprayed and heat-treated coatings. The heat-treated coating exhibited a homogenous microstructure, whereas the as-sprayed coating exhibited a non-homogenous microstructure comprising partially melted powder particles interconnected by regions that melted during spraying and re-solidified under cooling. The boundaries of the powder particles were highlighted by long, continuous pores and it was clear from the fracture patterns that crack propagation occurred along these boundaries. This type of crack propagation did not occur in

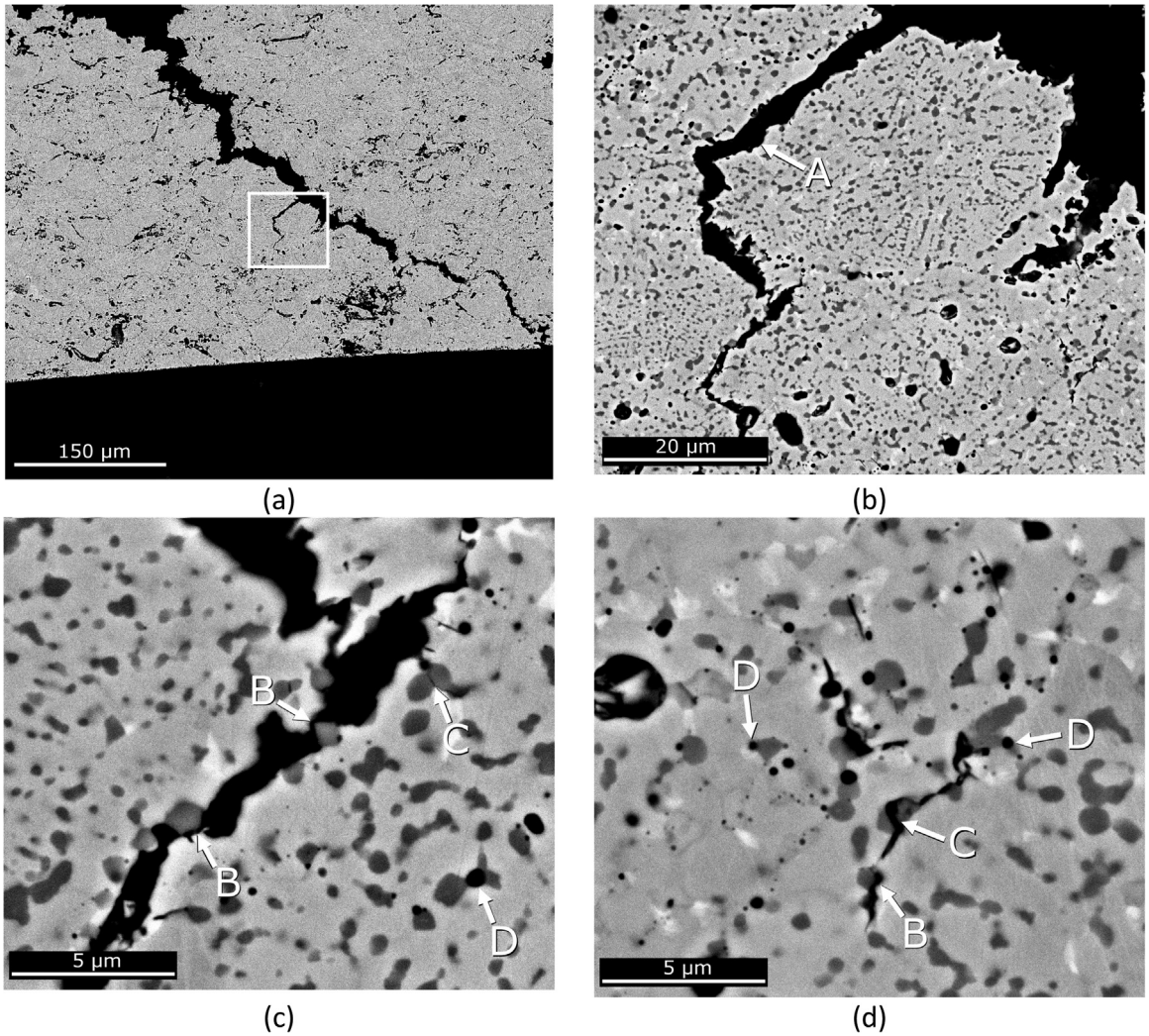

Fig. 10. BSE micrographs of the heat-treated Stellite 6 coating following SPC testing at 700 °C and 127 MPa. The letter A indicates cracking along a powder particle boundary, B indicates cracking along the carbide/matrix interface, C indicates cracking either through a carbide or along a carbide/carbide interface, and D indicates the growth of pores at the carbide/matrix and carbide/carbide interfaces.

the heat-treated coating as the long, continuous pores were removed during heat-treatment. The main mode of crack propagation in the heat-treated coating was cracking at the matrix/carbide interface. It is clear then that the increased creep resistance of the heat-treated coating is due to: (i) the precipitation of carbides; (ii) decrease in porosity, specifically the removal of the long, continuous pores; and (iii) decrease in hardness.

For both coatings, the growth of cracks can be attributed to strain mismatch between the different phases/regions within the coatings. This strain mismatch model has been used to explain the fracture behaviour of multi-phase materials such as dual-phase steels [46,47] and MCrAlY alloys [12]. Considering the heat-treated coating first, strain mismatch between the FCC matrix and the carbide phases caused a stress concentration at the interface and eventually led to the formation of voids during creep. The voids then developed into cracks which coalesced during tensile loading and caused specimen failure. Using a similar model for the as-sprayed coating, it can be assumed strain mismatch developed at the interface of the powder particles and the re-solidified regions. For the heat-treated coating, voids needed to form before the cracks developed, but for the as-sprayed coating, porosity already existed at the interface between phases. As such, cracking occurred much more readily in the as-sprayed coating resulting in a lower creep resistance.

Cracking was also observed in the as-sprayed coating at the dendrite phase boundaries within the powder particles. This cracking could be due to strain mismatch between either: an interdendritic phase, most likely a carbide, within the powder particles; or dendrites with significantly different grain orientation. In both instances, it appears the microstructure of the heat-treated coating is more creep resistant than the dendritic microstructure of the power particles in the as-sprayed coating. This is most likely due to the precipitation of the M_7C_3 and $M_{23}C_6$ type carbides in the heat-treated coating.

Despite the higher creep resistance of the heat-treated coating, the Norton power law parameter n, also known as the stress exponent, was similar for both coatings: 17.4 and 19.4 for the as-sprayed coating and heat-treated coating respectively. Stress exponents of 17–19 are much higher than those commonly observed for creep [48] but have been reported for small punch creep and uni-axial tensile testing of P92 steel [49,50]. In these studies, the plots of minimum steady-state strain rate vs stress for the P92 steel exhibited two distinct regions: a low-stress region with stress exponents in the range 4–8; and a high stress region with stress exponents in the range 12–17. The high stress exponents were attributed to a breakdown in creep strength within the high stress region. The times to failure ($< 10^3$ h) of the P92 steel in these studies [49,50] were similar to those observed for the as-sprayed and heat-treated Stellite 6 coatings. Hence, it is likely that the stress exponents for the Stellite 6 coatings represent a high-stress region in which the coatings are experiencing a breakdown in creep strength. This

breakdown in creep resistance may have been exacerbated by the macroscopic radial cracking observed on both coatings (Fig. 8). The radial cracking at low displacement did not cause immediate specimen failure for either coating because the cracks did not propagate further than the clamping boundary; however, it is likely that the creep resistance of both coatings was compromised after the onset of cracking and that the steady-state strain rates observed were likely higher than if cracking had not occurred. This may explain why both coatings exhibited high stress exponents and supports the assumption that both coatings experienced a breakdown in creep resistance; it can be assumed higher loads caused more significant cracking and therefore a more significant reduction in creep resistance, leading to high stress exponents. Hence, it is possible, although not confirmed in this study, that both the as-sprayed and heat-treated coatings would exhibit significantly lower stress exponents within a lower stress region.

In conclusion, the isothermal heat-treatment applied to the HVOF Stellite 6 coating significantly increased the coating's resistance to creep. The increased creep resistance can be attributed to the homogenisation of the microstructure, the precipitation of carbides accompanied by decrease in hardness and the removal of the long, continuous pores that existed at the powder particle boundaries in the as-sprayed coating.

6. Conclusions

- HVOF Stellite 6 coatings heat-treated at 1050 °C for 1 h under vacuum exhibit an FCC Co-Cr-W solid solution with 11 wt% and 7 wt % $M_{23}C_6$ and M_7C_3 carbides respectively. The heat treatment removed the HCP Co-based phase observed in the as-sprayed Stellite 6 coatings and reduced the level of porosity in the coatings.
- The heat-treated coatings exhibited small punch creep rates approximately 2 orders of magnitude lower than the as-sprayed coatings. This resulted in the heat-treated coatings exhibiting times to failure approximately 2 orders of magnitude longer than the as-sprayed coatings during small punch creep tests.
- Failure of the as-sprayed coatings during small punch creep testing was dominated by crack propagation along powder particle boundaries. Secondary crack propagation also occurred along dendrite phase boundaries within the powder particles that were retained in the as-sprayed coating.
- Failure of the heat-treated coatings was dominated by the formation of voids and cracking at the interface of the FCC Co-Cr-W solid solution and $M_{23}C_6/M_7C_3$ carbides. The formation of voids resulted from strain mismatch between the carbides and FCC matrix.

Acknowledgements

This work was supported by the Engineering and Physical Sciences Research Council [grant number EP/M01536X/1]. The authors would like to thank Rory Screaton for his assistance in HVOF spraying and Shane Maskill for his assistance in small punch creep testing. We would also like to thank the Nanoscale and Microscale Research Centre (NMRC) at the University of Nottingham for their assistance in microscopy.

Data availability

The raw/processed data required to reproduce these findings cannot be shared at this time as the data also forms part of an ongoing study.

References

[1] S. Bose, High Temperature Coatings, Butterworth-Heinemann, 2007.
[2] G.W. Goward, Progress in coatings for gas turbine airfoils, Surf. Coat. Technol. 108–109 (1998) 73–79.
[3] R. Rajendran, Gas turbine coatings – an overview, Eng. Fail. Anal. 26 (2012) 355–369.
[4] K.C. Antony, Wear-resistant cobalt-base alloys, J. Met. (1983).
[5] M. Riddihough, Stellite as a wear-resistant material, Tribology 3 (4) (1970) 211–215.
[6] A. Hjornhede, P. Sotkovszki, A. Nylund, Erosion-corrosion of laser and thermally deposited coatings exposed in fluidised bed combustion plants, Mater. Corros. 57 (4) (2006) 307–322.
[7] J. Rosler, M. Baker, M. Volgmann, Stress state and failure mechanisms of thermal barrier coatings: role of creep in thermally grown oxide, Acta Mater. 49 (2001) 3659–3670.
[8] D.S. Balint, J.W. Hutchinson, An analytical model of rumpling in thermal barrier coatings, J. Mech. Phys. Solids 53 (2005) 949–973.
[9] R. Darolia, Thermal barrier coatings technology: critical review, progress update, remaining challenges and prospects, Int. Mater. Rev. 58 (6) (2013) 315–348.
[10] H. Chen, T.H. Hyde, K.T. Voisey, D.G. McCartney, Application of small punch creep testing to a thermally sprayed CoNiCrAlY bond coat, Mater. Sci. Eng. A 585 (2013) 205–213.
[11] G.A. Jackson, W. Sun, D.G. McCartney, The influence of microstructure on the ductile to brittle transition and fracture behaviour of HVOF NiCoCrAlY coatings determined via small punch tensile testing, Materials Science and Engineering (2019) (In press).
[12] G.A. Jackson, Influence of Microstructure on the Mechanical Properties of Thermally Sprayed Nicocraly Coatings Determined by Small Punch Testing (Ph.D. thesis), University of Nottingham, Nottingham, UK, 2017.
[13] M. Eskner, R. Sandstrom, Mechanical properties and temperature dependence of an air plasma-sprayed NiCoCrAlY bondcoat, Surf. Coat. Technol. 200 (2006) 2695–2703.
[14] H. Brodin, M. Eskner, The influence of oxidation on mechanical and fracture behaviour of an air plasma-sprayed NiCoCrAlY bondcoat, Surf. Coat. Technol. 187 (2004) 113–121.
[15] M. Eskner, R. Sandstrom, Measurement of the ductile-to-brittle transition temperature in a nickel aluminide coating by a miniaturised disc bending test technique, Surf. Coat. Technol. 165 (2003) 71–80.
[16] M. Vostřák, J. Tesař, S. Houdková, E. Smazalová, M. Hruška, Diagnostic of laser remelting of HVOF sprayed Stellite coatings using an infrared camera, Surf. Coat. Technol. 318 (2017) 360–364.
[17] H. Hamatani, Y. Miyazaki, Optimization of an electron beam remelting of HVOF sprayed alloys and carbides, Surf. Coat. Technol. 154 (2002) 176–181.
[18] S. Houdková, Z. Pala, E. Smazalová, M. Vostřák, Z. Česánek, Microstructure and sliding wear properties of HVOF sprayed, laser remelted and laser clad Stellite 6 coatings, Surf. Coat. Technol. 318 (2017) 129–141.
[19] E. Lugscheider, C. Herbst, L. Zhao, Parameter studies on high-velocity oxy-fuel spraying of MCrAlY coatings, Surf. Coat. Technol. 108–109 (1998) 16–23.
[20] S. Saeidi, K.T. Voisey, D.G. McCartney, The effect of heat treatment on the oxidation behavior of HVOF and VPS CoNiCrAlY coatings, J. Therm. Spray. Technol. 18 (2) (2009) 209–216.
[21] S. Houdková, E. Smazalová, Z. Pala, Effect of heat treatment on the microstructure and properties of HVOF-sprayed Co-Cr-W coating, J. Therm. Spray. Technol. 25 (3) (2016) 546–557.
[22] Z. Pala, M. Bai, F. Lukac, T. Hussain, Laser clad and HVOF-sprayed Stellite 6 coating in chlorine-rich environment with KCl at 700 °C, Oxid. Met. 88 (5–6) (2017) 749–771.
[23] H.M. Rietveld, Line profiles of neutron powder-diffraction peaks for structure refinement, Acta Crystallogr. 22 (1) (1967) 151–152.
[24] G.A. Jackson, H. Chen, W. Sun, D.G. McCartney, The high temperature creep properties of a thermally sprayed CoNiCrAlY coating via small punch creep testing, Key Eng. Mater. 734 (2017) 37–48.
[25] CEN CWA 15627 Workshop Agreement: Small punch test method for metallic materials. European Committee for Standardization, Brussels, December, 2006.
[26] S.P. Jeffs, R.J. Lancaster, Elevated temperature creep deformation of a single crystal superalloy through the small punch creep method, Mater. Sci. Eng. A. 626 (2015) 330–337.
[27] Y. Li, M. Sun, C. Zhang, Practical approach to determine creep properties from small punch test, in: Proceedings of the 2nd International Conference Small Specimen Test Techniques: Determination of Mechanical Properties of Materials by Small Punch and Other Minature Testing Techniques, Ocelot, 2012, pp. 47–63.
[28] J. Chakrabarty, A theory of stretch forming over hemispherical punch heads, Int. J. Mech. Sci. 12 (1970) 315–325.
[29] G. Kong, D. Zhang, P.D. Brown, D.G. McCartney, S.J. Harris, Microstructural characterisation of high velocity oxy-fuel thermally sprayed Stellite 6, Mater. Sci. Technol. 19 (8) (2003) 1003–1011.
[30] P. Sassatelli, G. Bolelli, M.L. Gualtieri, E. Heinonen, M. Honkanen, L. Lusvarghi, T. Manfredini, R. Rigon, M. Vippola, Properties of HVOF-sprayed Stellite-6 coatings, Surf. Coat. Technol. 338 (2018) 45–62.
[31] C. Moreau, P. Cielo, M. Lamontagne, S. Dallaire, J.C. Krapez, M. Vardelle, Temperature evolution of plasma-sprayed niobium particles impacting on a substrate, Surf. Coat. Technol. 46 (2) (1991) 173–187.
[32] A. Frenk, W. Kurz, Microstructural effects on the sliding wear resistance of a cobalt-based alloy, Wear 174 (1994) 81–91.
[33] R.J. Lancaster, W.J. Harrison, G. Norton, An analysis of small punch creep behaviour in the gamma-titanium aluminide Ti-45Al-2Mn-2Nb, Mater. Sci. Eng. A. 274 (2015) (626-263).
[34] S. Rasche, M. Kuna, Improved small punch testing and parameter identification of ductile to brittle materials, Int. J. Press. Vessel. Pip. 125 (2015) 23–34.
[35] T.S. Sidhu, S. Prakash, R.D. Agrawal, Studies of the metallurgical and mechanical properties of high velocity oxy-fuel sprayed stellite-6 coatings on Ni- and Fe-based

superalloys, Surf. Coat. Technol. 201 (2006) 273–281.
[36] Y.C. Tsui, T.W. Clyne, An analytical model for predicting residual stresses in progressively deposited coatings part 1: planar geometry, Thin Solid Films 306 (1) (1997) 23–33.
[37] P.J. Withers, H.K.D.H. Bhadeshia, Residual stress. Part 1 – measurement techniques, Mater. Sci. Technol. 17 (4) (2001) 355–365.
[38] R. Ahmed, A. Ashraf, M. Elameen, N.H. Faisal, A.M. El-Sherik, Y.O. Elakwah, M.F.A. Goosen, Single asperity nanoscratch behaviour of HIPed and cast Stellite 6 alloys, Wear 312 (2014) 70–82.
[39] H. Yu, R. Ahmed, H. de Villiers Lovelock, S. Davies, Influence of manufacturing process and alloying element content on the tribomechanical properties of cobalt-based alloys, J. Tribol. 131 (2009) (011601 1-12).
[40] R. Singh, D. Kumar, S.K. Mishra, S.K. Tiwari, Laser cladding of Stellite 6 on stainless steel to enhance solid particle erosion and cavitation resistance, Surf. Coat. Technol. 251 (2014) 87–97.
[41] J.C. Shin, J.M. Dohb, J.K. Yoon, D.K. Lee, J.S. Kim, Effect of molybdenum on the microstructure and wear resistance of cobalt-base Stellite hardfacing alloys, Surf. Coat. Technol. 166 (2003) 117–126.
[42] V. Kuzucu, M. Ceylan, H. Celik, I. Aksoy, An investigation of Stellite-6 alloy containing 5.0 wt% silicon, J. Mater. Process. Technol. 79 (1998) 47–51.
[43] C.T. Sims, A contemporary view of cobalt-base alloys, J. Met. 21 (1969) 27–42.
[44] I.I. Superalloys, John Wiley & Sons, Inc, New York, 1987.
[45] Y.S. Lee, J. Yu, Effect of matrix hardness of the creep properties of a 12CrMoVNb steel, Metall. Mater. Trans. A 30 (9) (1999) 2331–2339.
[46] M. Calcagnotto, Y. Adachi, D. Ponge, D. Raabe, Deformation and fracture mechanisms in fine- and ultrafine-grained ferrite/martensite dual-phase steels and the effect of aging, Acta Mater. 59 (2011) 658–670.
[47] J. Kadkhodapour, A. Butz, S. Ziaei Rad, Mechanisms of void formation during tensile testing in a commercial, dual-phase steel, Acta Mater. 59 (7) (2011) 2575–2588.
[48] M.F. Ashby, D.R.H. Jones, Engineering Materials 1: An Introduction to Properties, Application and Design, 3rd ed., Butterworth-Heinemann, 2005.
[49] J.S. Lee, H.G. Armaki, K. Maruyama, T. Muraki, H. Asahi, Causes of breakdown of creep strength in 9Cr-1.8W-0.5Mo-VNb steel, Mater. Sci. Eng. A 428 (1–2) (2006) 270–275.
[50] V. Sklenicka, K. Kucharova, M. Svoboda, L. Kloc, J. Bursik, A. Kroupa, Long-term creep behaviour of 9-12% Cr power plant steels, Mater. Charact. 51 (1) (2003) 35–48.